Experimental investigation and thermodynamic modelling of the ThF$_4$-PuF$_3$ phase diagram

A. Tosolin [a,b], J.-F. Vigier [a], S. Mastromarino [a,c], R.J.M. Konings [a], L. Luzzi [b], O. Beneš [a,*]

[a] *Joint Research Centre, Karlsruhe, Germany*
[b] *Politecnico di Milano, Department of Energy, Via La Masa 34, Milan 20156, Italy*
[c] *Technical University Delft, Mekelweg 15, 2600 GA, Delft, The Netherlands*

HIGHLIGHTS

- First experimental results on the phase equilibria and phase stabilities in the ThF4-PuF3 system.
- New thermodynamic model for the ThF$_4$-PuF$_3$ system.
- *Re*-assessment of the ThF$_4$-PuF$_3$ and LiF-ThF$_4$-PuF$_3$ phase diagrams.
- Discussion on advantages and limitations of using proxy compounds to derive thermodynamic models from experimental data.
- Data contribute for extension and improvement of the JRCMSD thermodynamic database on molten halide systems.

ARTICLE INFO

ABSTRACT

Phase equilibria in the ThF$_4$-PuF$_3$ system were measured by differential scanning calorimetry. Samples were encapsulated to prevent leakage during the measurements and to prevent fluoride contamination of the instrument. Formation of intermediate compounds and solid solutions was investigated by X-ray diffraction. A thermodynamic model based on the CALPHAD approach was developed for the measured system. Good fit between measurements and phase equilibria calculated using the model was achieved.

1. Introduction

Thorium tetrafluoride (ThF$_4$) and plutonium fluoride (PuF$_3$) are considered as components of the nuclear fuel in some Molten Salt Reactor (MSR) designs, a group of innovative nuclear reactors, in which a molten mixture of salts (generally fluorides or chlorides) circulates in the primary system, operating as both coolant and nuclear fuel.

The employment of molten salts in nuclear reactors provides significant potential advantages in terms of safety and sustainability [1]. For these reasons, the Generation IV International Forum (GIF) selected the MSR amongst the six most promising innovative nuclear energy systems [2,3]. In this context, a consortium of European institutions has been working on the development of an innovative nuclear reactor concept called Molten Salt Fast Reactor (MSFR) [4], a large size nuclear reactor in which a mixture of actinide fluorides (including ThF$_4$ and PuF$_3$ for one of the fuel options under consideration [5]) is dissolved in enriched ^{7}LiF.

An extensive thermodynamic assessment of systems of interest for the MSFR is fundamental to evaluate issues concerning the safety of the reactor, such as (i) the formation of precipitates that may deposit in the primary circuit, potentially causing partitioning of fissile material; (ii) the minimum temperature at which the fuel is liquid; (iii) the optimal fuel composition; (iv) heat storage capacity of the fuel; (v) energy to melt the salt; (vi) volatility of radionuclides released from the fuel; and (vii) properties change if composition changes.

For a multi-component system, a systematic experimental approach may be difficult or not practical, due to the high number of possible combinations that need to be studied to achieve a broad understanding. However, thermodynamic calculations of multi-component systems can be performed starting from the assessment of its "pseudo-binary" sub-systems [6], assuming that thermodynamic functions and parameters for each of them are well-defined and correctly simulate the experimental evidence. Ternary and quaternary (or higher order) parameters can be implemented to obtain more accurate calculations.

In general, the system LiF-ThF$_4$-UF$_4$-PuF$_3$ can be used to study, select or optimize the initial fuel salt of the MSFR (or similar concepts) and its evolution during operation. Most of its binary sub-systems have been previously experimentally investigated [7–15], and thermodynamic models have been assessed following the CALPHAD approach.

In our previous work [16] we assessed the binary systems ThF$_4$-PuF$_3$ and UF$_4$-PuF$_3$ and two ternary systems LiF-ThF$_4$-PuF$_3$ and LiF-UF$_4$-PuF$_3$ using ThF$_4$ and CeF$_3$ as proxy compounds for UF$_4$ and PuF$_3$, respectively. This approach needs validation with PuF$_3$ and therefore new experimental results of the ThF$_4$-PuF$_3$ system are presented in this paper for the first time, together with a novel thermodynamic assessment for such system. The application of this approach to extrapolate phase diagrams using easier accessible inactive proxy compounds is discussed at the end of the paper by direct benchmarking.

The data obtained in this study provide direct contribution to improve the extensive thermodynamic database on molten salt reactor fuel and coolant systems, the JRCMSD (Joint Research Centre Molten Salt Database), which is accessible through the JRC Open Catalogue [17].

2. Experimental

2.1. Initial materials and handling of samples

ThF$_4$ and PuF$_3$ were synthesized at the Joint Research Centre (JRC) by hydrofluorination of the respective dioxides, in a facility specifically designed for fluorination of radioactive actinide materials [18]. In short, actinide nitrate solutions were added dropwise to an oxalic acid solution at room temperature to form the respective actinide oxalates. The precipitates were filtered, dried, and calcined to obtain actinide dioxides, which were then transformed to tetrafluorides by hydro-fluorination in a tube furnace, specially designed to work with HF gas.

Basic information of the synthesized materials is reported in Table 1, together with an estimation of the mass fraction purity, based on X-Ray Diffraction (XRD) and Differential Scanning Calorimetry (DSC) measurements. More details on the synthesis of ThF$_4$ and PuF$_3$ are provided in our previous works [15,18].

Both ThF$_4$ and PuF$_3$ salts are highly hygroscopic and sensitive to oxygen, which can yield oxides and oxyfluorides. To minimize potential contamination, the materials were stored and manipulated in argon glove boxes with a few ppm of oxygen and water. The synthesis/purification of the salts was performed in such glove boxes, as well as the preparation of the samples for all DSC measurements. All mixtures were prepared by mixing the end-members manually in an agate mortar. The quantity of each component was measured with a mass balance with a resolution of 0.1 mg. Then, the mixtures were encapsulated in DSC capsules, as described in the next section.

XRD measurements were performed in a nitrogen glove box with up to 2% of oxygen content. To prevent the samples from oxidation during the analysis the samples were embedded in epoxy resin, keeping exposure to oxygen and moisture very low.

As non-crystalline or low concentration (~1%) impurities would not be detected with XRD, this technique was coupled with DSC to verify component purity.

2.2. Differential scanning calorimetry

Phase transition temperatures were measured by DSC. The apparatus used was a Setaram high temperature calorimeter (MHTC 96) equipped with B-type thermocouples. Seventeen (17) different mixtures were prepared, starting from ThF$_4$-PuF$_3$ (97–3 mol%) and increasing the amount of PuF$_3$ using steps of 5 mol%. To prevent vaporization of the sample at high temperature, to avoid sample contamination, and to protect the device from corrosive fluoride vapours, samples were encapsulated in stainless steel crucibles with a nickel liner to assure chemical compatibility. Each capsule was filled with approximately 50–70 mg of salt mixture, sealed by a nickel plate pressed by two sharp edges of the main crucible which ensured hermetical tightness. The capsule was designed to fit the sample compartments of our DSC apparatus, as shown in Fig. 1. More details about the encapsulation are provided in our previous work [19].

The DSC experimental chamber was evacuated and purged by helium gas twice prior each experiment to eliminate possible impurities which may affect the measurement. During the experiments, the experimental chamber was flushed with a slight flow of helium (15 ml/min) to avoid possible oxidation. As the material of the crucibles was stainless steel, the maximum temperature reached during the DSC measurements was 1543 K.

The same device was also used to confirm purity of the initial materials prior to the preparation of the samples. For ThF$_4$, the purity check was performed by melting point determination and comparing results with literature values [18,20] (a single component salt would yield a single DSC peak whereas a contaminated specimen would likely yield multiple peaks). The melting point was determined by taking the onset point of the peak formed upon melting (1383 ± 2 K) in the DSC heat flow signal. An excellent agreement with literature value was found confirming the high purity of ThF$_4$ used as starting material.

Due to the very high melting point of PuF$_3$ (1705 ± 10 K) [21,22] which e, the purity check of PuF$_3$ was performed measuring the melting point of the eutectic mixture LiF-PuF$_3$ (79–21 mol%) and comparing results to literature values [13,15]. Lithium fluoride for this test was obtained from Alfa Aesar, which declares a metal-based purity of 99.99%. The material was dried before the use under argon at 623 K for 4 h to remove residual moisture and afterwards it was subjected to purity check by melting point determination using DSC. As the measurement of the dried LiF product confirmed the same melting point as the reference value, and the heat flow signal of the DSC indicated no signs of impurities, we considered the product as pure.
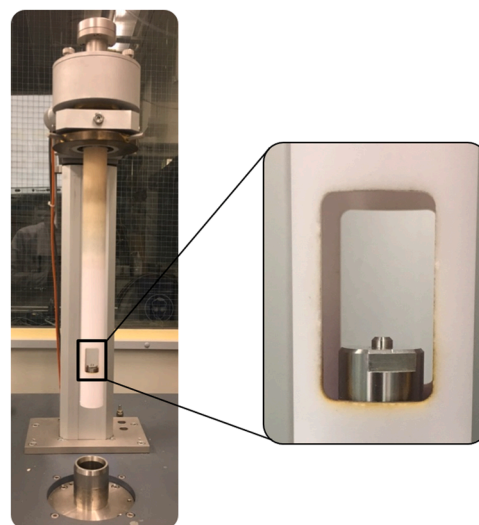

Fig. 1. Photograph of insertion of the stainless steel capsule into the DSC compartments.

Table 1
Basic information of ThF$_4$ and PuF$_3$ used in this work.

Chemical Formula	IUPAC Name	CAS Reg. No.	Source	Mass fraction purity / %
ThF$_4$	Tetrafluorothorium	13,709–59–6	Synthesized	> 99.0 [a]
PuF$_3$	plutonium; trifluoride	13,842–83–6	Synthesized	> 99.0 [a]

[a] Indicative value based on XRD and melting point determination by DSC.

The DSC was calibrated using the melting point of a series of reference materials (Sn, Pb, Zn, Al, Ag, Cu), which were inserted in the same crucible used for the experiments but using a boron nitride liner instead of the nickel one, to avoid alloying. We note that a series of previous benchmarking experiments showed that no observable temperature deviations were found when switching between nickel or boron nickel liner and therefore the calibration was appropriate for our experimental campaign.

Each DSC experiment consisted of three heating ramps at 10 K/min, up to approximately 100 K above the expected liquid points, based on thermodynamic calculations performed using the model developed in our previous work [16]. The first ramp was to achieve a good mixing between the end-members, the second ramp was to collect values from the measurement, and the third ramp to assess repeatability. Acquisition and post-processing of the data were carried out using the Calisto software v1.10. The temperature corresponding to the formation of $PuTh_2F_{11}$ and the solidus temperature were determined from the respective onset points of the related peaks on the DSC curve upon heating. The liquidus temperature was determined from the offset point of the broader peak, which appeared as a change of slope on the DSC curve. Since XRD was performed after cooling and we noted the presence of a metastable phase (Section 4.2), information of cooling rate is also important, which in this work was 10 K/min.

2.3. X-Ray diffraction

The XRD device used in this study was a Bruker D8 Bragg-Brentano Advance diffractometer (Cu Kα1 radiation) equipped with a curved Ge (1,1,1) monochromator and a LynxEye Linear Position Sensitive detector. The diffractometer working potential and current were 40 kV and 40 mA, respectively. Powder diffraction patterns were recorded across an angular range $10° \leq 2\theta \leq 120°$. Refinements of the patterns were done using Jana 2006 crystallographic software [23]. Only lattice parameters were refined, and atomic positions fixed based on available literature data. In case of $PuTh_2F_{11}$, since this compound has not been reported in literature, the atomic positions were fixed the values reported for the isostructural $SmTh_2F_{11}$ [24].

XRD analysis was performed on some post-DSC samples to assess formation of possible compounds and solid solutions during the DSC experiments. To retrieve the material from the DSC crucibles, a circular blade was used to cut the capsule, and the material was scraped out with a thin flathead screwdriver. The cutting was only possible in a nitrogen glove box, in which the saw is installed. Since the atmosphere in the nitrogen glove boxes contains higher concentrations of oxygen and moisture compared to the argon ones, the open sample was transferred immediately after cutting, minimizing the time of exposure. It is also important to note that the open sample was in frozen bulk form, so the intake of potential oxygen or moisture from impure atmosphere is much slower compared to e.g., its powder form and had no effect on the post-XRD analysis.

XRD samples were prepared by embedding approximately 50 mg of recovered sample into an epoxy resin, which was first homogenised by manual grinding in an agate mortar.

3. Thermodynamic modelling

A new thermodynamic assessment was developed for the ThF_4-PuF_3 system using the FactSage software [25]. The assessment was done by optimizing the thermodynamic excess Gibbs energy parameters of solid and liquid solutions and the standard enthalpy and entropy term at 298 K for the intermediate compound $PuTh_2F_{11}$. The initial values subjected to optimization were taken from our earlier study [16], in which a thermodynamic assessment of the ThF_4-PuF_3 system was made based on a proxy-system where CeF_3 was used as a surrogate.

According to the CALPHAD approach, the optimization of the unknown parameters was done to best fit the available, i.e. the measured, experimental data. For a binary solution, the total Gibbs energy function is generally defined as [6]:

$$G(T) = x_1 G_1(T) + x_2 G_2(T) + x_1 RT \ln x_1 + x_2 RT \ln x_2 + G^{xs} \qquad (1)$$

in which x_1 and x_2 are the mole fractions of the end-members, and R is the gas constant. The first two terms $x_1 G_1(T)$ and $x_2 G_2(T)$ refer to Gibbs energy contributions of pure end-members. The third and fourth terms $x_1 RT \ln x_1$, resp. $x_2 RT \ln x_2$ refer to configurational entropy of an ideal mixing. The latter term G^{xs} is the contribution due to the non-ideal mixing, and considers the possible repulsive and attractive forces between the end-members. G^{xs} is difficult to measure and it is generally optimized from phase diagram data for solid and liquid solutions. We note here that the configurational entropy term for the liquid solution treated in this work is modified according to the quasi-chemical model description published in series of papers by Pelton and Chartrand [26–29] and is defined as:

$$\Delta S^{conf.} = -R(n_A \ln X_A + n_B \ln X_B)$$
$$-R\left(n_{AA}\ln\frac{X_{AA}}{Y_A^2} + n_{BB}\ln\frac{X_{BB}}{Y_B^2}\right) + n_{AB}\ln\left(\frac{X_{AB}}{2Y_A Y_B}\right) \qquad (2)$$

in which n_A and n_B are number of moles of A and B cations (in our case, Pu^{3+} and Th^{4+}), n_{AA}, n_{BB} and n_{AB} are number of moles of corresponding pairs. X_A and X_B are mole fractions of A, resp. B cations, X_{ij} $(i,j = A,B)$ pair fractions. The cationic and anionic mole fractions are defined as:

$$GX_A = 1 - X_B = \frac{n_A}{(n_A + n_B)} \qquad (3)$$

resp.

$$X_{ij} = \frac{n_{ij}}{(n_{ij} + n_{ii} + n_{jj})} \qquad (4)$$

Y_A and Y_B terms in Eq. (2) are the so-called coordination-equivalent fractions defined as:

$$Y_A = 1 - Y_B = \frac{Z_{AB}^A X_A}{(Z_{AB}^A X_A + Z_{AB}^B X_B)} \qquad (5)$$

with Z_{AB}^A and Z_{AB}^B being cation-cation coordination numbers which define composition of the strongest short-range ordering in the studied system. The values for the unary pairs (Pu^{3+}-Pu^{3+} and Th^{4+}-Th^{4+}) used in this study have been taken from our previous study by Capelli et al. [16] (this is also needed to assure compatibility amongst all sub-systems in the multicomponent database), while for the Pu-Th binary pair the cation-cation coordination numbers were selected to reproduce the maximum short range order around eutectic composition, thus around 33mol% of ThF_4. All used $Z_{ij/FF}$ cation-cation coordination numbers are reported in Table 2 for prompt view.

The Gibbs energy function for a pure compound is defined as follows:

$$G(T) = \Delta_f H^0(298) - S^0(298)T + \int_{298}^{T} C_p(T)dT - T\int_{298}^{T}\frac{C_p(T)}{T}dT \qquad (6)$$

in which $\Delta_f H^0(298)$ and $S^0(298)$ are the standard enthalpy of formation and the standard absolute entropy referring to a temperature of 298.15 K. $C_p(T)$ is the molar heat capacity at constant pressure.

For solid solutions, a sub-lattice model [16] was used considering the

Table 2
Cation-cation coordination numbers of the liquid solution.

A	B	$Z_{AB/FF}^A$	$Z_{AB/FF}^B$
Pu^{3+}	Pu^{3+}	6	6
Th^{4+}	Th^{4+}	6	6
Pu^{3+}	Th^{4+}	6	3

cationic species (Th^{4+} and Pu^{3+}) on the first sub-lattice, and the anionic species (F^-) on the second sub-lattice. In this model, the cationic (y_A, y_B, …) and anionic (y_X, y_Y, …) fractions are defined as follows:

$$y_A = q_A n_A / (q_A n_A + q_B n_B + \ldots) \tag{7}$$

$$y_X = q_X n_X / (q_X n_X + q_Y n_Y + \ldots) \tag{8}$$

where n_i are the moles of ion i in solution, and q_i are the absolute ionic charges. The excess Gibbs energy for a binary solution with a common ion $A,B/F$ is function of the cationic and anionic fractions:

$$\Delta g^{xs} = \sum_{i \geq 1} \sum_{j \geq 1} y_A^i \, y_B^j \, L_{i,j} \tag{9}$$

where $L_{i,j}$ is the interaction parameter to be optimized.

For liquid solutions, the modified quasi-chemical model [26–29] was used. The model is based on the Second Nearest Neighbour (SNN) interaction approximation: if A and B are two cations (e.g., Th and Pu) and F is the fluorine anion, the formation of the SNN pair can be written as:

$$(A - F - A) + (B - F - B) = 2(A - F - B) \; \Delta g_{AB/FF} \tag{10}$$

where $\Delta g_{AB/FF}$ is the Gibbs energy of the pair exchange reaction. This parameter is determined empirically to achieve a good fit with experimental results.

$$\Delta g^{xs} = \Delta g^0_{AB/FF} + \sum_{i \geq 1} g^i_{AB/FF} \chi^i_{AB/FF} + \sum_{j \geq 1} g^j_{AB/FF} \chi^j_{BA/FF} \tag{11}$$

in which $\Delta g^0_{AB/FF}$ and $g^{ij}_{AB/FF}$ are composition independent coefficients, even though they may depend on temperature. The variation of $\Delta^i g_{AB/FF}$ with respect to the composition is represented by $\chi_{AB/FF}$ and $\chi_{BA/FF}$ coefficients, defined as follows:

$$\chi_{AB/FF} = \left(\frac{X_{AA}}{X_{AA} + X_{AB} + X_{BB}} \right);$$
$$\chi_{BA/FF} = \left(\frac{X_{BB}}{X_{AA} + X_{AB} + X_{BB}} \right), \tag{12}$$

in which X_{AA}, X_{AB} and X_{BB} are the cation-cation pair fractions.

4. Results and discussion

4.1. Differential scanning calorimetry

DSC heat flow signals for ThF$_4$-PuF$_3$ samples typically showed three phase transitions. By way of example, the heat flow signal upon heating for the composition ThF$_4$-PuF$_3$ (47–53 mol%) is shown in Fig. 2. The phase transition at the lowest temperature corresponds to the formation of the intermediate compound PuTh$_2$F$_{11}$, as predicted in our previous work [16] and confirmed by XRD analysis (discussed in Section 4.2) on post-DSC samples in this work. This is also consistent with the work by Abaouz et al. [24], who synthesized and characterized the similar compound LnTh$_2$F$_{11}$ (Ln = La–Lu, Y). The formation of PuTh$_2$F$_{11}$ occurs above 1178 K and is visible in the heat flow curve as a broad peak.

The other phase transitions indicated in Fig. 2 correspond to the solidus and liquidus transitions. In general, the reading of the onset and offset temperatures was quite challenging for many of the measured samples, as the phase transitions resulted in broad peaks. This is especially true for the liquidus point determination. For this reason, an uncertainty of ± 10 K was applied to eutectoids and eutectic type of equilibria and ± 20 K for liquidus equilibria. Results for all measured compositions are listed in Table 3.

The eutectic composition (composition with lowest melting point) is ThF$_4$-PuF$_3$ (72–28 mol%), at which solidus and liquids correspond. The melting temperature for this composition was measured 1253 $\pm$ 10 K.
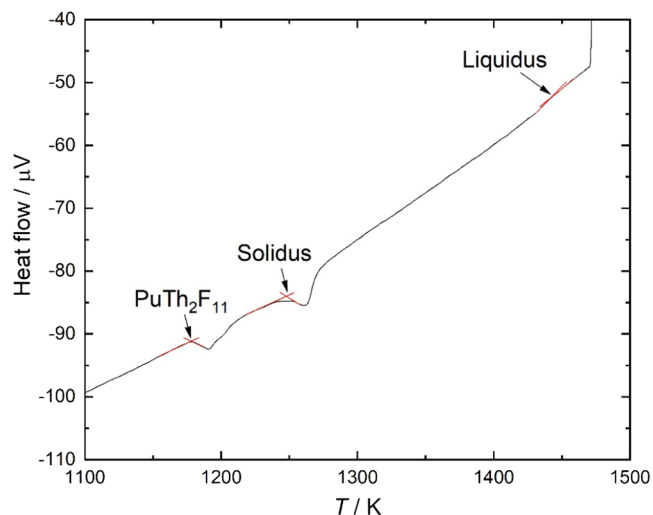

Fig. 2. DSC signal for the composition ThF$_4$-PuF$_3$ (47–53 mol%) and determination of the onset and offset points corresponding to the formation of PuTh$_2$F$_{11}$ (first onset point), the solidus (second onset point) and the liquidus (change of slope).

Table 3

Phase transition temperatures of the ThF$_4$-PuF$_3$ system measured by DSC. Uncertainty on temperature is $\pm$ 10 K for eutectoid and eutectics, and $\pm$ 20 K for liquidus.

x PuF$_3$	Equilibrium	T / K	x PuF$_3$	Equilibrium	T / K
0.03	Eutectoid	1180	0.43	Eutectic	1265
0.03	Eutectic	1251	0.43	Liquidus	1370
0.03	Liquidus	1377	0.48	Eutectoid	1178
0.08	Eutectoid	1180	0.48	Eutectic	1252
0.08	Eutectic	1246	0.48	Liquidus	1408
0.08	Liquidus	1355	0.53	Eutectoid	1176
0.13	Eutectoid	1180	0.53	Eutectic	1248
0.13	Eutectic	1253	0.53	Liquidus	1438
0.13	Liquidus	1335	0.58	Eutectoid	1183
0.18	Eutectoid	1180	0.58	Eutectic	1246
0.18	Eutectic	1259	0.58	Liquidus	1482
0.18	Liquidus	1319	0.63	Eutectoid	1183
0.23	Eutectoid	1182	0.63	Eutectic	1245
0.23	Eutectic	1255	0.63	Liquidus	1506
0.23	Liquidus	1281	0.68	Eutectoid	1184
0.28	Liquidus	1253	0.68	Eutectic	1247
0.28	Eutectic	1182	0.68	Liquidus	1533
0.33	Eutectoid	1175	0.73	Eutectoid	1192
0.33	Eutectic	1255	0.73	Eutectic	1253
0.33	Liquidus	1297	0.78	Eutectoid	1188
0.38	Eutectoid	1182	0.78	Eutectic	1250
0.38	Eutectic	1252	0.83	Eutectoid	1186
0.38	Liquidus	1330	0.83	Eutectic	1247
0.43	Eutectoid	1178			

It should be noted that since our instrument could not reach the melting temperature of one of the end-members (PuF$_3$), we have no direct proof that all mixtures with PuF$_3$ content 73 mol% or lower (those for which a liquidus transition was detected) fully melted homogenously inside the capsules. However, we observed a very good repeatability of the measurements, and the heat flow signals (following the first heating ramp) were generally "clean" with no unexpected peaks. This suggests that the mixtures inside the capsules were melted and homogeneous. For samples with PuF$_3$ content 73 mol% or higher the liquidus transition was outside the measurement range, so the mixtures inside the capsules were probably not fully melted.

For compositions with PuF$_3$ content higher than 83 mol% no phase transition was detected in the DSC heat flow curves. As shown in Fig. 3 for the composition ThF$_4$-PuF$_3$ (10–90 mol%), no peaks appeared even
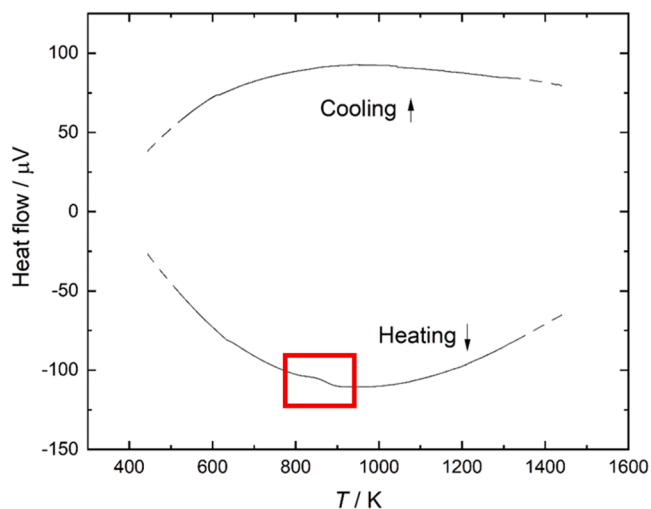
Fig. 3. DSC curves during the heating (bottom) and the cooling (top) for the composition ThF$_4$-PuF$_3$ (10–90 mol%).

during the cooling curve, which generally gives a more evident signal for the liquidus transition. However, detailed analysis of the curve during the heating showed that a broad peak occurred between 800 and 900 K. This observation, plus the absence of the solidus phase transition, suggested the formation of a solid solution on the PuF$_3$ side of the phase diagram. This was also suggested in the phase diagram by Capelli et al. [16], who made similar experiments using CeF$_3$ as a proxy compound of PuF$_3$. XRD studies were performed to confirm the presence of this large solid solution on the PuF$_3$ side (Section 4.2).

4.2. X-ray diffraction

The XRD pattern of the sample with composition ThF$_4$-PuF$_3$ (10–90 mol%) recorded after DSC measurement is presented in Fig. 4. The pattern shows a single phase with the space group *P*-3*c*1, also reported for pure PuF$_3$ [15]. This result confirmed the formation of a solid solution between ThF$_4$ and PuF$_3$ at this composition, as suggested by the DSC observations described above. Compared to pure PuF$_3$ (a(PuF$_3$) = 7.095 Å and c(PuF$_3$) = 7.257 Å) [15], dissolution of 10% of ThF$_4$ in PuF$_3$ is responsible of a contraction of the lattice in *a* direction and a dilatation in *c* direction.
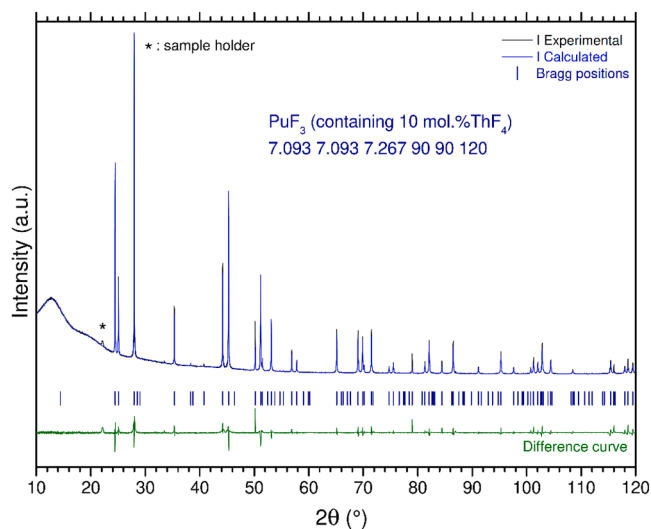
The room temperature XRD analyses of the ThF$_4$-PuF$_3$ (67–33 mol% or the stoichiometric phase PuTh$_2$F$_{11}$) composition revealed three phases, namely ThF$_4$, PuF$_3$ and PuTh$_2$F$_{11}$ (Fig. 5).

The presence of about 20% of PuTh$_2$F$_{11}$ in the material after DSC measurement suggests the metastable nature of this compound at room temperature, which does not fully dissociate into ThF$_4$ and PuF$_3$. This observation is supported by the work of Abaouz et al. [24], who studied LnTh$_2$F$_{11}$ compounds for a large range of rare earth compositions (Ln = La–Lu, Y) and pointed out their metastable nature. Abaouz et al. [24] also reported that these compounds are isostructural and provided atomic positions of SmTh$_2$F$_{11}$ from single crystal diffraction technique. The Rietveld refinement performed in our study fixed the atomic positions of PuTh$_2$F$_{11}$ based on SmTh$_2$F$_{11}$. By comparing the values of lattice volumes of LnTh$_2$F$_{11}$ series from Abaouz et al. [24] with the one of PuTh$_2$F$_{11}$ from our study, the volume of PuTh$_2$F$_{11}$ lattice is in good agreement regarding the ionic radii provided by Shannon [30], as shown in Fig. 6.

It is worthwhile noticing that despite an initial composition of ThF$_4$-PuF$_3$ (67–33 mol%), the amount of PuF$_3$ phase detected after DSC measurement is higher than the ThF$_4$ phase. This tends to indicate that certain proportion of ThF$_4$ is dissolved in the PuF$_3$ crystal phase, which is in agreement with the formation of ThF$_4$-PuF$_3$ (10–90 mol%) solid solution described above. The lattice parameter of PuF$_3$ phase in post DSC sample ThF$_4$-PuF$_3$ (67–33 mol%) showed further contraction of the lattice in the *a* direction and further dilatation in the *c* direction compared to ThF$_4$-PuF$_3$ (10–90 mol%) solid solution, which suggests that the amount of ThF$_4$ dissolved in PuF$_3$ phase is significantly higher than 10 mol%.

4.3. ThF$_4$-PuF$_3$ phase diagram - modelling

For the optimization of the ThF$_4$-PuF$_3$ phase diagram, the thermodynamic data for ThF$_4$ and PuF$_3$ end-members were taken from Capelli et al. [16], while the data for the intermediate PuTh$_2$F$_{11}$ compound were optimized. In absence of a measured value, the heat capacity PuTh$_2$F$_{11}$ was estimated from the end-members using the Neuman-Kopp rule, while standard enthalpy and absolute entropy, both referenced to 298.15 K, were optimized to best fit the compound stability limits determined by the DSC experiments. The thermodynamic data of the PuTh$_2$F$_{11}$ compound used in this work are:

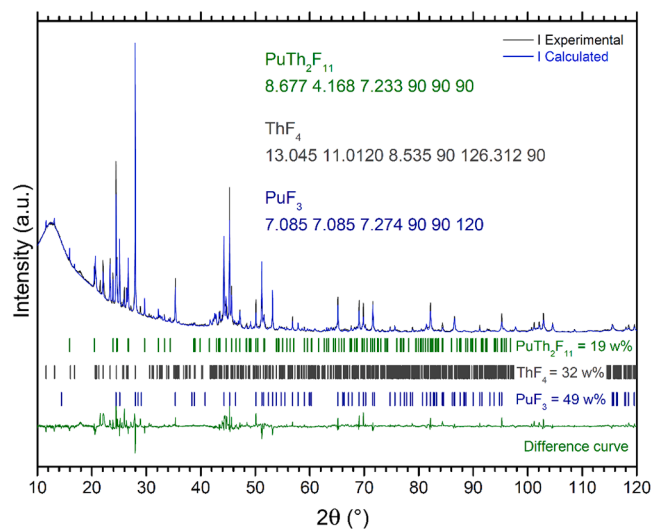$$\Delta H^{\circ}(298) = -5742.3 \text{ kJ} \cdot \text{mol}^{-1} \tag{13}$$

Fig. 4. XRD pattern of post DSC sample with composition ThF$_4$-PuF$_3$ (10–90 mol%).

Fig. 5. XRD pattern of post DSC sample with composition ThF$_4$-PuF$_3$ (67–33 mol% i.e. stoichiometric PuTh$_2$F$_{11}$).
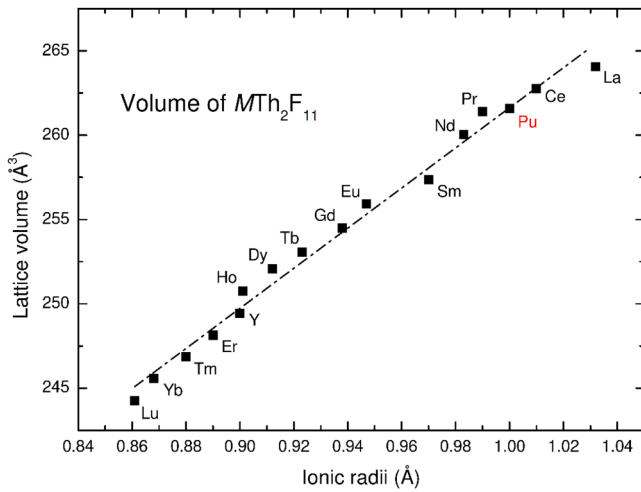
Fig. 6. Variation of $LnTh_2F_{11}$ (Ln = La to Lu) lattice volume reported from Abaouz [24] and $PuTh_2F_{11}$ (our study) as a function of ionic radii [30].

$$S^{\circ}(298) = 447 \text{ J·K}^{-1}\text{·mol}^{-1} \tag{14}$$

$$C_p(T) = 348.424 + 0.017447 \cdot T - 3,545,500 \cdot T^2 \text{ J·K}^{-1}\text{·mol}^{-1} \tag{15}$$

Optimization of the excess Gibbs energy functions for solid and liquid solutions were made manually to achieve agreement with the experimental phase equilibrium data measured in this study. Following the notation used in eq. (9) and (11), the optimized excess Gibbs energy functions used in this work are:

$$\Delta g^{xs}(s.s.) = y_{Pu}^1 \, y_{Th}^3 \, 70,000 \text{ J·mol}^{-1} \tag{16}$$

$$\Delta g^{xs}(liq.) = -3000 - 1900\chi_{PuTh/F} \text{ J·mol}^{-1} \tag{17}$$

for the solid (*s.s.*) and liquid solution (*liq.*), respectively.

Implementing these values to the thermodynamic functions previously proposed by Capelli et al. [16], the ThF_4-PuF_3 phase diagram was re-assessed. The calculated phase diagram is shown in Fig. 7 together with experimental results listed in Table 3, showing very good general agreement.

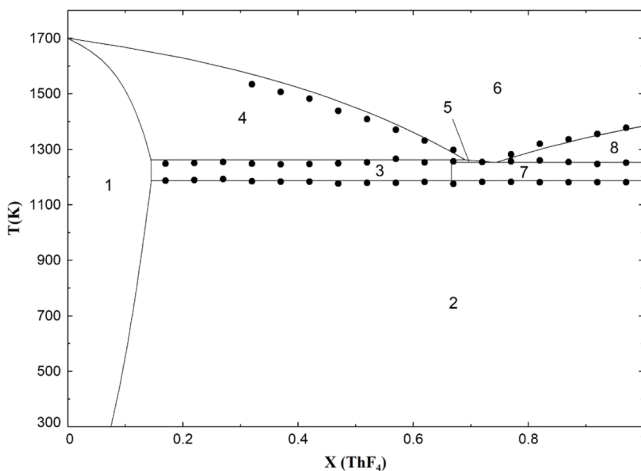The phase diagram shows extensive solid solution on the PuF_3 side

Fig. 7. The ThF_4-PuF_3 phase diagram. (●) Data measured in this study. Uncertainty on the measured points is ±10 K. Solid line, data calculated in this work. (1) $(Pu_{1-x}Th_x)F_{3+x}$ solid solution; (2) ThF_4 + $(Pu_{1-x}Th_x)F_{3+x}$ solid solution; (3) $(Pu_{1-x}Th_x)F_{3+x}$ solid solution + $PuTh_2F_{11}$; (4) $(Pu_{1-x}Th_x)F_{3+x}$ solid solution + liquid; (5) $PuTh_2F_{11}$ + liquid; (6) liquid; (7) ThF_4 + $PuTh_2F_{11}$; (8) ThF_4 + liquid.

with maximum ThF_4 solubility at 14.5 mol%, and the formation of $PuTh_2F_{11}$ at 1187 K. The eutectic and peritectic points are calculated at 1252 K and X(ThF_4) = 0.75 mol%, resp. 1261 K and X(ThF_4) = 0.69 mol %.

4.4. ThF_4-PuF_3 phase diagram – comparison to the surrogate model

It has been highlighted in the introduction section that this study provides the first experimental data on the phase equilibria of the ThF_4-PuF_3 system, which is the basis for the novel thermodynamic assessment of the ThF_4-PuF_3 phase diagram. It has been further mentioned that in our earlier study by Capelli et al. [16] the same phase diagram has been already assessed but based on excess Gibbs parameters taken from the optimization of the model for the surrogate ThF_4-CeF_3 system. As one of the outcomes of this study is to assess how reliable estimations of phase diagrams can be achieved using this 'surrogate' type of approach, we compare the two obtained phase diagrams in Fig. 8. In the figure the bold lines are the present ThF_4-PuF_3 phase diagram based on the experimental data measured in this work, while the thin lines represent phase equilibria based on our previous estimation. From a closer look, we can derive the following conclusions:

- There is general good agreement between the two phase diagrams: the liquidus line slope agrees very well and both phase diagrams show the same stabilized chemical species in the solid state, i.e. solid solution on the PuF_3 rich side and the Th_2PuF_{11} intermediate compound. Especially the latter is worth highlighting, as the surrogate ThF_4-CeF_3 system from the work of Capelli et al. [16] contained in addition the $ThCeF_7$ phase, which in the case of PuF_3-containing system was not found as stable.
- Some discrepancies have been found comparing the two phase diagrams; (i) the stability of the PuF_3-based solid solution was somewhat overestimated using the surrogate model, and (ii) the eutectic point was underestimated in the surrogate version, lower by 55 K.

The above observations demonstrate that the method of using the excess Gibbs parameters form surrogate systems can lead to very good first approximation of phase diagrams, useful for exploring fuel salt compositions. At the same time, we strongly recommend treating such results with caution when performing design and safety calculations for which experimental validation is essential.

4.5. LiF-ThF_4-PuF_3 re-assessment

With the novel data presented in this study and the novel thermodynamic assessment of the ThF_4-PuF_3 system, the full LiF-ThF_4-PuF_3 fuel system has been re-assessed. To best fit the experimental data on solubility of PuF_3 in two LiF-ThF_4 (80–20 mol%) and LiF-ThF_4 (78–22 mol%) solvent measured by Ignatiev et al. [31], ternary excess Gibbs energy parameters of the liquid solution had to be optimized. The obtained ternary parameters somewhat differ to our earlier study by Capelli et al. [16], which was assessed based on the CeF_3 surrogate systems, and become:

$$\Delta g_{LiTh(Pu)} = -8253.4 \text{ J·mol}^{-1} \tag{18}$$

$$\Delta g_{ThPu(Li)} = 20920 \text{ J·mol}^{-1} \tag{19}$$

A comparison between the solubility data calculated based on the assessed data and the experimental data by Ignatiev et al. is given in Fig. 9, showing a very good match for both studied solvent compositions.

The calculated liquidus projection of the obtained LiF-ThF_4-PuF_3 system is shown in Fig. 10 indicating 6 ternary invariant equilibria (in the figure, E denotes eutectic and Q denotes quasi-peritectic). The type of equilibria and the corresponding temperature with composition is
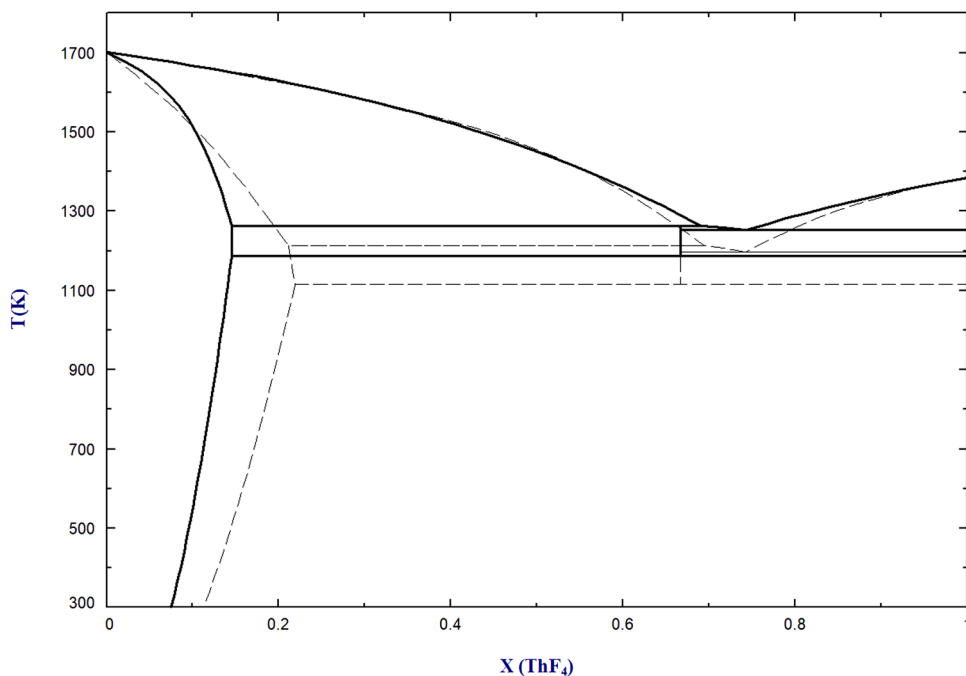
Fig. 8. Comparison between the assessed ThF₄-PuF₃ phase diagram (solid line) and the one estimated based on the surrogate ThF₄-CeF₃ system (dashed line) taken from our previous work by Capelli et al. [16].
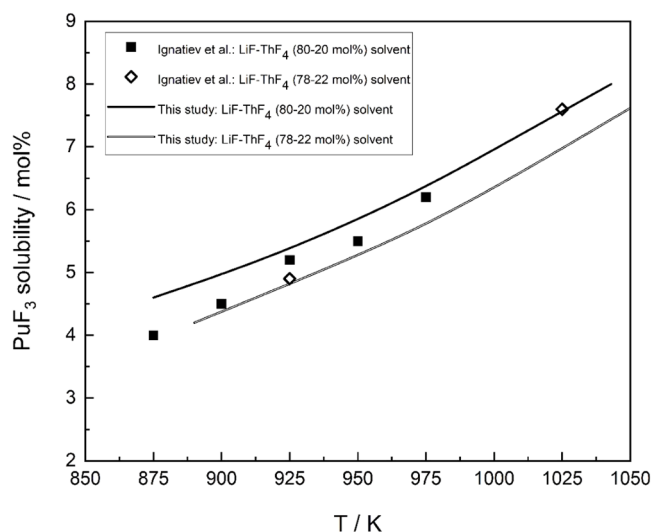

Fig. 9. Solubility of PuF₃ in LiF–ThF4 mixtures calculated as function of temperature. ■ and ◇ Experimental data of the PuF₃ solubility in the LiF–ThF₄ (80–20 mol%), resp. LiF–ThF₄ (78–22 mol%) solvents measured by Ignatiev et al. [31].

given in Table 4. One saddle point is found between the two eutectics, at T = 825.1 K and molar ratio composition: X(LiF) = 0.733, X(ThF₄) = 0.244, X(PuF₃) = 0.023.

5. Conclusions

The ThF₄-PuF₃ phase diagram was investigated experimentally for the first time. 17 different compositions were measured by DSC to identify phase equilibria in the system. The formation of PuTh₂F₁₁ intermediate compound and solid solution at PuF₃ rich side of the phase diagram were confirmed by XRD analysis on post-DSC samples.

Experimental results were used to improve thermodynamic model predictions of the ThF₄-PuF₃ pseudo-binary system according to
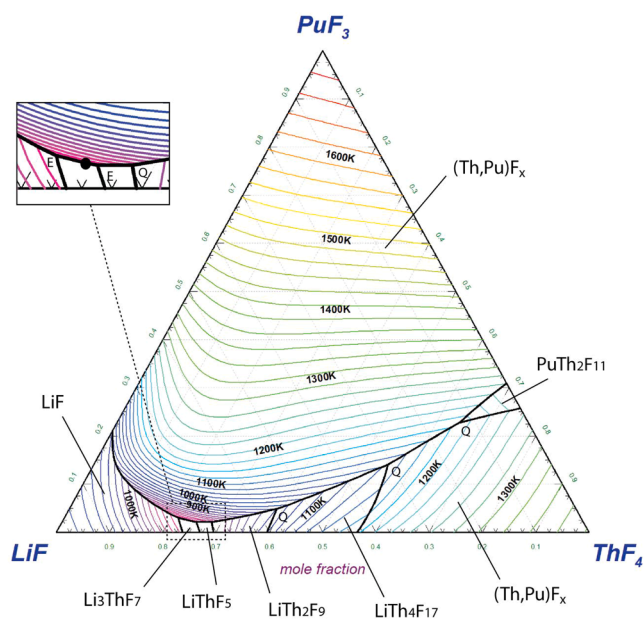

Fig. 10. Calculated liquidus projection of the LiF-ThF₄-PuF₃ system, re-assessed in this work based on the novel data obtained for the ThF₄-PuF₃ sub-system.

Table 4
Calculated ternary invariant equilibria found in the re-assessed LiF-ThF₄-PuF₃ system.

Invariant Equilbria	X (LiF)	X (ThF₄)	X (PuF₃)	T / K
Eutectic	0.755	0.213	0.032	819.4
Eutectic	0.726	0.251	0.023	822.7
Quasi-Peritectic	0.697	0.280	0.023	863.6
Quasi-Peritectic	0.561	0.389	0.050	1020.0
Quasi-Peritectic	0.309	0.550	0.141	1121.7
Quasi-Peritectic	0.130	0.643	0.227	1186.6

CALPHAD approach, and good agreement between calculations and measurements was achieved. Furthermore, this study shows that very reliable estimations of actinide containing phase diagrams can be achieved using optimized thermodynamic parameters of their surrogate systems (which are generally easier accessible), but it also shows that these estimates must be treated with larger uncertainty and experimental studies are key for phase diagram improvement or validation.

This work is a significant contribution to complete the thermodynamic assessment of the LiF-ThF$_4$-UF$_4$-PuF$_3$ system, which is one of the key fluoride-based MSR fuel system. At the same time, the assessed data provide a valuable contribution to the JRCMSD database describing the key fluoride and chloride-based MSR fuel and coolant systems.

CRediT authorship contribution statement

A. Tosolin: Conceptualization, Methodology, Validation, Formal analysis, Investigation, Writing – original draft, Writing – review & editing. **J.-F. Vigier:** Methodology, Validation, Formal analysis, Investigation, Writing – original draft, Writing – review & editing. **S. Mastromarino:** Methodology, Validation, Formal analysis, Investigation. **R.J.M. Konings:** Conceptualization, Writing – review & editing. **L. Luzzi:** Writing – review & editing. **O. Beneš:** Conceptualization, Methodology, Validation, Formal analysis, Investigation, Writing – original draft, Writing – review & editing.

Declaration of Competing Interest

There is no conflict of interest for me and other authors.

Data availability

Data will be made available on request.

Acknowledgements

References

[1] J. Serp, M. Allibert, O. Beneš, S. Delpech, O. Feynberg, V. Ghetta, D. Heuer, D. Holcomb, V. Ignatiev, J.L. Kloosterman, L. Luzzi, E. Merle-Lucotte, J. Uhlíř, R. Yoshioka, D. Zhimin, The molten salt reactor (MSR) in generation IV: overview and perspectives, Prog. Nucl. Energy 77 (2014) 308–319, https://doi.org/10.1016/j.pnucene.2014.02.014.

[2] US DOE Nuclear Energy Research Advisory Committee and the Generation IV International Forum, A technology roadmap for generation IV nuclear energy systems, 2002, Report GIF-002-00. 10.2172/859029.

[3] I. Pioro, Handbook of Generation IV Nuclear Reactors, Woodhead Publishing, 2016.

[4] M. Allibert, M. Aufiero, M. Brovchenko, S. Delpech, V. Ghetta, D. Heuer, A. Laureau, E. Merle-Lucotte, Molten salt fast reactors, Woodhead Publish. Series Energy (2016) 157–188, https://doi.org/10.1016/B978-0-08-100149-3.00007-0.

[5] M. Brovchenko, D. Heuer, E. Merle-Lucotte, M. Allibert, V. Ghetta, A. Laureau, P. Rubiolo, Design-related studies for the preliminary safety assessment of the molten salt fast reactor, Nucl. Sci. Eng. 175 (2013) 329–339, https://doi.org/10.13182/NSE12-70.

[6] N. Saunders, A.P. Miodownik (Eds.), CALPHAD (Calculation of Phase Diagrams): A Comprehensive Guide, Volume 1, Pergamon, 1998.

[7] R.E. Thoma, H. Insley, B.S. Landau, H.A. Friedman, W.R. Grimes, Phase equilibria in the fused salt systems LiF–ThF$_4$ and NaF–ThF$_4$, J. Phys. Chem. 63 (1959) 1266–1274, https://doi.org/10.1021/j150578a013.

[8] E. Capelli, O. Beneš, M. Beilmann, R.J.M. Konings, Thermodynamic investigation of the LiF-ThF$_4$ system, J. Chem. Thermodyn. 58 (2013) 110–116, https://doi.org/10.1016/j.jct.2012.10.013.

[9] C.J. Barton, H.A. Friedman, W.R. Grimes, H. Insley, R.E. Moore, R.E. Thoma, Phase equilibria in the alkali fluoride-uranium tetrafluoride fused salt systems: I, The systems LiF-UF$_4$ and NaF-UF$_4$, J. Am. Ceram. Soc. 41 (1958) 62–84, https://doi.org/10.1111/j.1151-2916.1958.tb15446.x.

[10] C.F. Weaver, R.E. Thoma, H. Insley, H.A. Friedman, Phase equilibria in the systems UF$_4$-ThF$_4$ and LiF-UF$_4$-ThF$_4$, J. Am. Ceram. Soc. 43 (1960) 213–218, https://doi.org/10.1111/j.1151-2916.1960.tb12984.x.

[11] J.P.M. van der Meer, R.J.M. Konings, H.A.J. Oonk, Thermodynamic assessment of the LiF–BeF$_2$–ThF$_4$–UF$_4$ system, J. Nucl. Mater. 357 (2006) 48–57, https://doi.org/10.1016/j.jnucmat.2006.05.042.

[12] O. Beneš, M. Beilmann, R.J.M. Konings, Thermodynamic assessment of the LiF-NaF-ThF$_4$-UF$_4$ system, J. Nucl. Mater. 405 (2010) 186–198, https://doi.org/10.1016/j.jnucmat.2010.08.017.

[13] C.J. Barton, R.A. Strehlow, Phase relations in the system LiF-PuF$_3$, J. Inorg. Nucl. Chem. 18 (1961) 143–147, https://doi.org/10.1016/0022-1902(61)80381-3.

[14] O. Beneš, R.J.M. Konings, Actinide burner fuel: potential compositions based on the thermodynamic evaluation of MF-PuF$_3$ (M = Li, Na, K, Rb, Cs) and LaF$_3$-PuF$_3$ systems, J. Nucl. Mater. 377 (2008) 449–457, https://doi.org/10.1016/j.jnucmat.2008.04.004.

[15] A. Tosolin, P. Souček, O. Beneš, J.F. Vigier, L. Luzzi, R.J.M. Konings, Synthesis of plutonium trifluoride by hydro-fluorination and novel thermodynamic data of PuF$_3$-LiF system, J. Nucl. Mat. 503 (2018) 171–177, https://doi.org/10.1016/j.jnucmat.2018.02.037.

[16] E. Capelli, O. Beneš, R.J.M. Konings, Thermodynamic assessment of the LiF-ThF$_4$-PuF$_3$-UF4 system, J. Nucl. Mater. 462 (2015) 43–53, https://doi.org/10.1016/j.jnucmat.2015.03.042.

[17] Joint Research Centre Molten Salt Database - JRCMSD, (n.d.). https://joint-research-centre.ec.europa.eu/joint-research-centre-molten-salt-database-jrcmsd_en (accessed May 25, 2023).

[18] P. Souček, O. Beneš, B. Claux, E. Capelli, M. Ougier, V. Tyrpekl, J.F. Vigier, R.J.M. Konings, Synthesis of UF$_4$ and ThF$_4$ by HF gas fluorination and re-determination of the UF$_4$ melting point, J. Fluor. Chem. 200 (2017) 33–40, https://doi.org/10.1016/j.jfluchem.2017.05.011.

[19] O. Beneš, R.J.M. Konings, S. Wurzer, M. Sierig, A. Dockendorf, A DSC study of the NaNO$_3$-KNO$_3$ system using an innovative encapsulation technique, Thermochim Acta 509 (2010) 62–66, https://doi.org/10.1016/j.tca.2010.06.003.

[20] R.J.M. Konings, E. van del Meer, E. Walle, Chemical Aspects of Molten Salt Reactor Fuel and Coolant – Tech. Rep., ITU-TN 2005/25 (2005), Eggenstein-Leopoldshafen, Germany.

[21] A. Tosolin, J.Y. Colle, S. Mastromarino, P. Souček, L. Luzzi, R.J.M. Konings, O. Beneš, Vaporization behaviour of a PuF$_3$-containing fuel mixture for the molten salt fast reactor, J. Nucl. Mater. 527 (2019), 151780, https://doi.org/10.1016/j.jnucmat.2019.151780.

[22] E.F. Westrum, J.C. Wallmann, The melting point and the heat of sublimation of plutonium trifluoride, J. Am. Chem. Soc. 73 (1951) 3530–3531, https://doi.org/10.1021/ja01151a535.

[23] V. Petrícek, M. Dušek, L. Palatinus, Crystallographic computing system JANA2006: general features, Zeitschruplet Fur Kristallographie 229 (2014) 345–352, https://doi.org/10.1515/zkri-2014-1737.

[24] A. Abaouz, A. Taoudi, J.P. Laval, Synthesis and characterization of a metastable LnTh$_2$F$_{11}$ Series (Ln=La–Lu, Y) with cationic and anionic disorder: crystal structure of SmTh$_2$F$_{11}$, J. Solid State Chem. 130 (1997) 277–283, https://doi.org/10.1006/jssc.1997.7327.

[25] C.W. Bale, E. Bélisle, P. Chartrand, S.A. Decterov, G. Eriksson, A.E. Gheribi, K. Hack, I.H. Jung, Y.B. Kang, J. Melançon, A.D. Pelton, S. Petersen, C. Robelin, J. Sangster, P. Spencer, M.A. Van Ende, FactSage thermochemical software and databases, 2010–2016, Calphad 54 (2016) 35–53, https://doi.org/10.1016/j.calphad.2016.05.002.

[26] A.D. Pelton, S.A. Degterov, G. Eriksson, C. Robelin, Y. Dessureault, The modified quasichemical model I—Binary solutions, Metall. Mater. Trans. B 31 (2000) 651–659, https://doi.org/10.1007/s11663-000-0103-2.

[27] A.D. Pelton, P. Chartrand, The modified quasi-chemical model: part II. Multicomponent solutions, Metall. Mater. Trans. A 32 (2001) 1355–1360, https://doi.org/10.1007/s11661-001-0226-3.

[28] P. Chartrand, A.D. Pelton, The modified quasi-chemical model: part III. Two sublattices, Metall. Mater. Trans. A 32 (2001) 1397–1407, https://doi.org/10.1007/s11661-001-0229-0.

[29] A.D. Pelton, P. Chartrand, G. Eriksson, The modified quasi-chemical model: part IV. Two-sublattice quadruplet approximation, Metall. Mater. Trans. A Phys. Metall. Mater. Sci. 32 (2001) 1409–1416, https://doi.org/10.1007/s11661-001-0230-7.

[30] R.D. Shannon, Revised effective ionic radii and systematic studies of interatomic distances in halides and chalcogenides, Acta Crystallogr., Sect. A 32 (1976) 751–767, https://doi.org/10.1107/S0567739476001551.

[31] V. Ignatiev, O. Feynberg, A. Merzlyakov, A. Surenkov, A. Zagnitko, V. Afonichkin, A. Bovet, V. Khokhlov, V. Subbotin, R. Fazilov, M. Gordeev, A. Panov, A. Toropov, Progress in development of MOSART concept with the support, in: Proceedings of ICAPP, Chicago, 2012.